UC Davis

UC Davis Previously Published Works

Title

Prediction of Urban Air Mobility Multirotor VTOL Broadband Noise Using UCD-QuietFly

Permalink

https://escholarship.org/uc/item/7vt580jb

Journal

Journal of the American Helicopter Society, 66(3)

ISSN

0002-8711

Authors

(Kevin) Li, Sicheng

Lee, Seongkyu

Publication Date

2021-07-01

DOI

10.4050/jahs.66.032004

Peer reviewed

eScholarship.org Powered by the California Digital Library
University of California

Prediction of Urban Air Mobility Multirotor VTOL Broadband Noise Using UCD-QuietFly

Sicheng (Kevin) Li*
Ph.D. Candidate

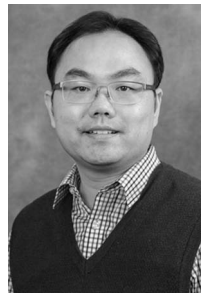

Seongkyu Lee
Associate Professor

University of California, Davis, CA

This paper investigates broadband noise of multirotor urban air mobility (UAM) vertical take-off and landing (VTOL) vehicles. Based on an earlier single-rotor trailing-edge noise prediction method, a multirotor broadband noise prediction program is developed, where the multirotor coordinate transformation is included, and the amplitude modulation capability is introduced. Thereafter, the program is used to predict broadband noise from three UAM VTOL conceptual designs and a vertiport conceptual design. It is found that UAM VTOL vehicles' broadband noise is important in the high-frequency range, where the community background noise level is typically low. For the same mission specifications, broadband noise is found to be higher for VTOL designs with more rotors. UAM vehicle noise is compared to conventional helicopter noise. It is found that the amplitude modulation of broadband noise of a single rotor is insignificant when the observer distance is larger than four rotor radii. Multirotor vehicles at the same rotational speeds have weaker amplitude modulations than a single rotor, which demonstrates the benefits of using multiple rotors in terms of noise annoyance. Finally, noise contours from a vertiport design show an increase in the broadband noise level when multiple VTOL vehicles are operated simultaneously.

Nomenclature

C_f	skin friction coefficient
C_T	thrust coefficient
c	chord length, m
c_o	speed of sound, m/s
D	rotor diameter, m
D_ϕ	directivity term
dp/dx	pressure gradient, Pa/m
E^*	complex conjugate of a Fresnel integral
f	frequency, Hz
k_x	chordwise wavenumber, 1/m
L	effective lift function, N/m
l_r	spanwise turbulence lengthscale, m
M	freestream Mach number
M_r	rotational Mach number
M_t	rotor tilt motion matrix
M_{tip}	tip Mach number
M_{β_p}	flapping motion matrix
M_θ	blade twist and collective pitch matrix
M_ϕ	azimuth motion matrix
N_B	number of blades
N_R	number of rotors
N_S	number of sections per blade
R	rotor radius, m
R_o	observer-hub distance, m
R_s	observer-blade section distance, m
r	radial position of a blade section midspan, m
S_{pp}	azimuthally averaged acoustic PSD, Pa^2/Hz
$\bar{S}_{pp}$	instantaneous acoustic PSD, Pa^2/Hz
t_r	rotor tilt, deg
t_v	vehicle tilt, deg
U_0	rotor forward velocity, m/s
U_c	convective velocity, m/s
U_e	boundary layer edge velocity, m/s
U_∞	freestream velocity, m/s
u_τ	friction velocity, $(\tau_w/\rho)^{1/2}$, m/s
V_c	ascending speed, m/s
X, Y, Z	source local coordinate system, m
X_1, Y_1, Z_1	rotor coordinate system, m
X_2, Y_2, Z_2	observer global coordinate system, m
α_{tpp}	rotor tip path plane angle referenced to forward velocity, deg
β_p	blade flap, deg
Δr	blade section span, m
δ	boundary layer thickness, m
δ^*	boundary layer displacement thickness, m
Θ	momentum thickness, m
θ	blade twist, deg
θ_0	collective pitch, deg
μ	advance ratio, $U_0/\Omega R$
ν	kinematic viscosity, m^2/s

*Corresponding author; email: sili@ucdavis.edu

Presented at the 2020 VFS Aeromechanics for Advanced VerticalFlight Technical Meeting, San Jose, CA, January 21–23, 2020. Manuscript received June 2020; accepted February 2021.

 © 2021 Vertical Flight Society

ρ	fluid density, kg/m^3
σ	rotor solidity
τ_w	wall shear stress, Pa
Φ_{pp}	surface pressure spectrum, Pa^2/Hz
ϕ	blade azimuth angle, deg
Ψ	elevation angle, deg
Ω	rotor rotational speed, rad/s
ω	source frequency, rad/s
ω_d	Doppler-shifted frequency, rad/s
OASPL	overall sound pressure level, dB
PWL	sound power level, dB
$SPL_{i(U/L)}$	blade section (upper or lower surface) sound pressure level, dB
SPL_{rotor}	rotor sound pressure level, dB
$SPL_{vehicle}$	vehicle sound pressure level, dB

Introduction

Broadband noise from rotorcraft is characterized by its wide frequency range and high-frequency dominance. Historically, rotorcraft broadband noise has received less attention compared to its discrete-frequency, or tonal, noise. However, as the concepts of urban air mobility (UAM) have recently become more prominent, rotorcraft broadband noise has gained more interest due to its impact on urban residents. Specifically, Intaratep et al. (Ref. 1) demonstrated on a DJI Phantom drone that its broadband noise not only dominates the mid- to high-frequency noise spectrum, but the noise level is also significantly increased from the single-rotor to the multirotor configuration. Regarding the noise perception, Zawodny and Boyd (Ref. 2) showed the importance of high-frequency rotor broadband noise on the A-weighted sound pressure level (SPL).

Trailing-edge noise is a type of broadband noise that contributes significantly to mid- and high-frequency noise. This noise is generated by the interaction between a turbulent boundary layer flow and a trailing-edge corner on an airfoil section or a flat plate. Trailing-edge noise models on an airfoil have been empirically and theoretically developed. A semiempirical Brooks-Pope-Marcolini (BPM) model was developed by Brooks et al. (Ref. 3) and has been widely used to predict airfoil self-noise. Theoretically, Ffowcs Williams and Hall (Ref. 4) provided a trailing-edge noise solution to the Lighthill (Ref. 5) acoustic analogy equation. Likewise, using the theory of Curle (Ref. 6), Amiet (Ref. 7) developed a theoretical model to predict trailing-edge noise on an airfoil. Using Amiet's model, Schlinker and Amiet (Ref. 8) predicted trailing-edge noise on helicopters, but some simplifications were made in their approach. For example, helicopter blades were modeled as flat plates; induced velocity on the rotor was not included; noise sources were located at the rotor hub. Using the rotating source formulation of Ffowcs Williams and Hawkings (Ref. 9), Kim and George (Ref. 10) predicted rotor trailing-edge noise with the loading function in Amiet's model (Ref. 7). In their method, however, each blade was modeled as a point source of a flat plate, and the angle of attack effect was neglected. Modeling rotor blades as actual airfoil sections, Blandeau and Joseph (Ref. 11) predicted propeller trailing-edge noise based on Amiet's model (Ref. 7), but the wall pressure spectrum model, Goody's model (Ref. 12), used in their approach was not accurate for airfoil adverse pressure gradient flows, and the noise source was modeled as a point source located at 75% of the blade radius. Li and Lee (Ref. 13) presented a new method to predict rotor trailing-edge broadband noise, which combined blade element momentum theory (BEMT), XFOIL panel method (Ref. 14), Lee's wall pressure spectrum model (Refs. 15, 16), and Amiet's trailing-edge noise model (Ref. 7), and considers rotor blades' full motions. The rotorcraft aerodynamics was solved by the BEMT to obtain the local velocity and angle of attack along the blade span. For each blade section, the far-field noise was obtained from the Amiet trailing-edge noise model, which required the coordinate transformations to include rotor blade motions. Although Zawodny et al. (Ref. 17) and Pettingill and Zawodny (Ref. 18) have predicted broadband noise from small-scale rotors using the semiempirical BPM model (Ref. 3), broadband noise from the passenger-size electric vertical take-off and landing (eVTOL) vehicles has not been predicted, nor has the vehicle designs been studied for their effects on the broadband noise.

Regarding the noise characteristics, Christian et al. (Ref. 19) used a synthesizing method with the BPM model to simulate the amplitude-modulated broadband noise from a helicopter, which became more identifiable by its periodic features. However, the importance of such features has not been studied for the multirotor VTOL vehicles. Regarding the VTOL designs, Johnson et al. (Ref. 20) made conceptual designs of single passenger quadrotor, six-passenger side-by-side helicopter, and fifteen-passenger tilt-wing and turbo-electric aircraft. Based on these designs, Silva et al. (Ref. 21) produced three new designs, quadcopter, side-by-side, and lift+cruise, with the same mission specifications of carrying six passengers. These conceptual designs are given in Fig. 1. The specifications of the three conceptual designs are shown in Table 1. Silva et al. (Ref. 21) presented the electric and turbo-electric versions of each VTOL design, and in this paper the electric versions are studied. However, the broadband noise has not been predicted on these designs.

The constitution of VTOL/UAM noise sources is shown in Fig. 2. While VTOL/UAM community noise consists of various sources, such as the flow, mechanical vibration, and motor, the dominant noise pertinent to the community acceptance mainly comes from aerodynamically induced noise or flow noise. While VTOL/UAM community noise consists of various sources, such as the flow, mechanical vibration, and motor, an important noise component pertinent to the community acceptance is aerodynamically induced noise or flow noise. Flow noise is dominated by noise emitted from the rotor blades, although airframe also marginally contributes (Ref. 2). Generated from the blades, tonal noise dominates the low frequencies while the broadband noise dominates the mid to high frequencies. While Jia and Lee (Refs. 22, 23) investigated VTOL tonal blade–vortex interaction (BVI) noise, this paper will focus on broadband noise of recently designed UAM VTOL configurations for the first time. Although broadband blade–wake interaction (BWI) noise is dominant at the low and mid frequencies in descending flight, broadband airfoil self-noise is dominant at the mid to high frequencies in hover and forward flight (Ref. 24), in which BWI is weak. An exemplary A-weighted noise spectrum containing UAM VTOL noise sources is shown in Fig. 3. Among the airfoil self-noise sources, trailing-edge noise is dominant, which makes it a good representation of mid- to high-frequency UAM VTOL noise.

To investigate such topics, this paper extends the authors' earlier work and the capability of a computer program, UCD-QuietFly (Ref. 13), which introduces the capability of predicting broadband noise from multirotor vehicles. This program is used to predict broadband noise of the VTOL conceptual designs (Ref. 21) in Fig. 1; the importance of VTOL broadband noise is studied by comparing to the urban community noise measurements (Ref. 25). Furthermore, the significance of periodic features of VTOL broadband noise is studied at various observer locations. Finally, broadband noise of multiple operating VTOLs at one of Uber's considered vertiport design (Ref. 26) is predicted. It is important to note that rotor broadband noise considered in this paper includes trailing-edge noise, trailing-edge bluntness noise, and airfoil stall noise, which are important at mid- to high-frequency range. In this paper, other broadband noise sources, such as BWI noise or turbulence ingestion noise, which are apparent in a low-frequency region, are not considered.

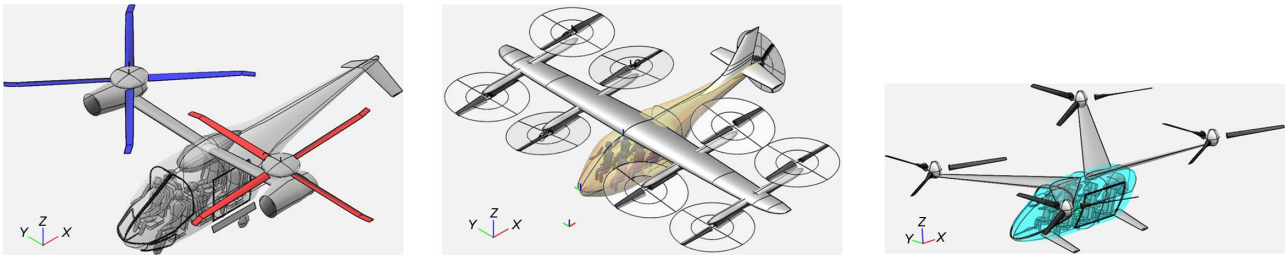

(a) (b) (c)

Fig. 1. NASA's six-passenger UAM VTOL conceptual designs (Ref. 21): (a) side-by-side, (b) lift+cruise, and (c) quadcopter.

Table 1. Parameters of UH-1B helicopter and six-passenger UAM VTOL conceptual designs (Ref. 21)

Parameter	UH-1B	Quadrotor	Side-by-Side	Lift+Cruise
Rotor radius (ft)	22	13.1	14.9	5.0
Number of rotors	1	4	2	8
Blades per rotor	2	3	4	2
Tip speed (ft/s)	748.031	550	550	585
Rotor speed (RPM)	325	400	353	1117
Disk loading (lb/ft^2)	4.74	3.0	3.5	13.1
Solidity, thrust-weighted	0.0036	0.055	0.058	0.267
Airfoils	NACA0012	VR-12 (r/R<0.85)/SSC-A09 (r/R>0.95)		

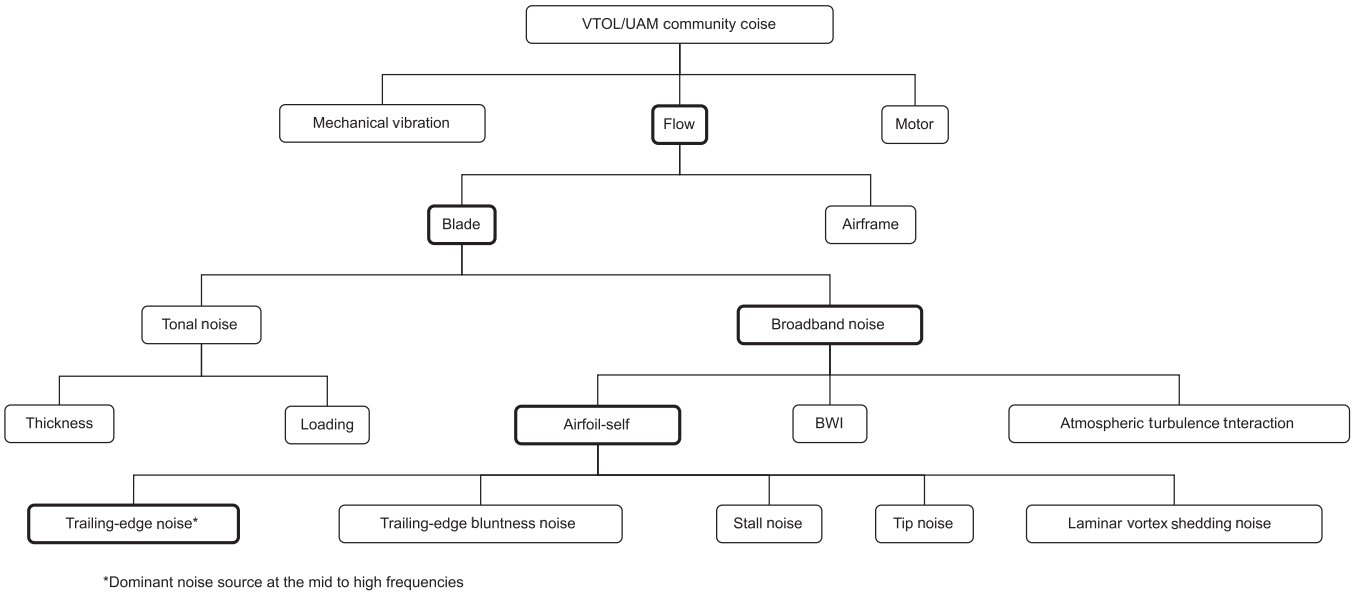

Fig. 2. UAM VTOL community noise sources and classifications.

Method and Formulation

Multirotor broadband noise

In addition to a single-rotor prediction capability of UCD-QuietFly presented in Ref. 13, the multirotor broadband noise prediction capability is included in this paper to investigate UAM VTOL vehicles. In addition, the amplitude modulation capability is employed to study the time-dependent characteristics of the UAM VTOL broadband noise.

UCD-QuietFly is a physics-based method that relates the far-field acoustics with the turbulent pressure fluctuations near the trailing edge through the theory of edge scattering (Ref. 6). Therefore, UCD-QuietFly not only predicts rotor broadband noise but also contains fundamental flow physics of the noise generation, which helps improve the physical understanding of noise generation and incorporate noise reduction techniques, such as trailing-edge serrations, into the model.

Besides the rotor trailing-edge noise, a capability of predicting the trailing-edge bluntness noise and the stall noise is added using the semiempirical BPM model (Ref. 3). It is important to note that the separation noise described in the BPM model still physically describes trailing-edge noise at nonzero angles of attack. For airfoils that are not stalled, this effect is also captured in our trailing-edge prediction based on the Amiet model (Ref. 7); the BPM stall noise model is only used on the stalled blade sections, which rarely occur in normal conditions. These capabilities are intended to cover more noise sources belonging to rotor broadband noise, although trailing-edge noise is found to be the

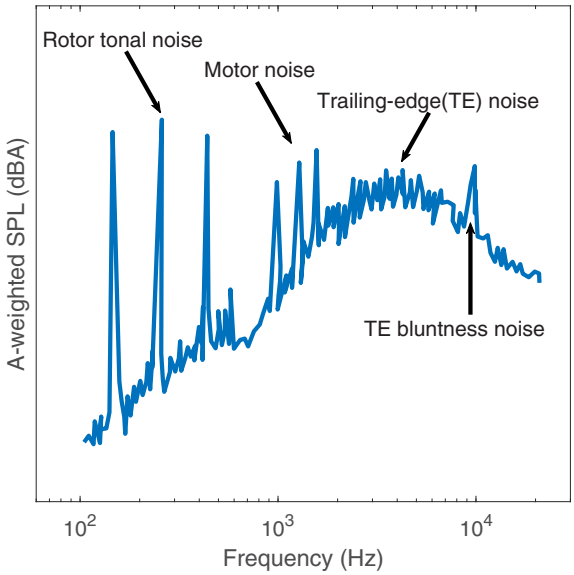

Fig. 3. Schematic A-weighted noise spectrum of UAM VTOL rotors. Note that the relative importance of each noise component can vary with the operating condition.

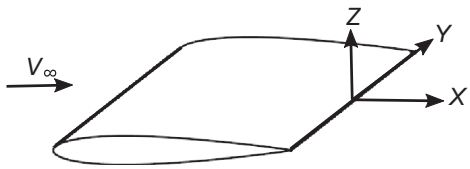

Fig. 4. Blade section local coordinate (Ref. 13).

dominant source. However, the current UCD-QuietyFly does not include a model for predicting turbulent wake/blade interaction broadband noise, which is more prominent at low frequencies during the onset. As for the amplitude modulation, the azimuthal averaging of the rotor trailing-edge noise is replaced by recording the narrow-band SPL in the history of time steps. Since the blade sections have different positions with respect to the observer at an observer time, the retarded-time effect is also considered.

Using the Schwarzschild solution (Ref. 27), Amiet's power spectral density (PSD) $\overline{S}_{pp}$ (Ref. 7) at an observer location (X, Y, Z) with respect to each of the two surfaces of an airfoil is written as

$$\overline{S}_{pp} = \frac{1}{32\pi^2}\left(\frac{\omega_d c Z}{c_o \epsilon^2}\right)^2 \Delta r |L|^2 l_r \Phi_{pp} \tag{1}$$

The overbar on S_{pp} means the acoustic power spectrum density from an airfoil section. In Eq. (1), $\epsilon^2 = X^2 + \beta^2(Y^2 + Z^2)$, $\beta^2 = 1 - M^2$, ω_d is the Doppler-shifted frequency, c is the chord length, c_o is the speed of sound, Δr is the blade sectional span, L is the loading term, l_r is the spanwise turbulence correction length, and Φ_{pp} is the wall pressure spectrum at 99% of c. The local coordinates used in Eq. (1) is shown in Fig. 4. On a rotor blade, the origin of the local coordinate of each section is located at its midspan.

Figure 5 shows the coordinates of a blade section on a rotor relative to an observer. The coordinate transformation matrices for each rotor are essentially the same as the single rotor UCD-QuietFly method (Ref. 13) as shown in Eqs. (2) and (3), where the tilt angle matrix M_t is modified to include multiple rotors on a vehicle, since each rotor can have different tilt angles. The definitions of t_v and t_r are described in the next paragraph. It should be noted that Eqs. (2) and (3) be performed on each rotor. These matrices transform the rotor coordinate (X_1, Y_1, Z_1) at the rotor hub to

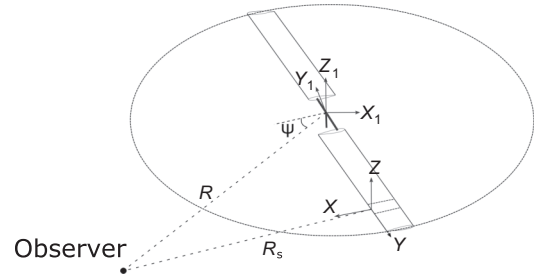

Fig. 5. Airfoil local and global coordinates for an observer (Ref. 13). Positive elevation angle is defined as above the rotor.

the local coordinate (X, Y, Z) on a blade section.

$$\begin{bmatrix} X \\ Y \\ Z \end{bmatrix} = M_\theta M_\phi \left(M_t \begin{bmatrix} X_1 \\ Y_1 \\ Z_1 \end{bmatrix} + M_{\beta_p} \right) \tag{2}$$

$$\begin{aligned} M_\theta &= \begin{bmatrix} \cos(\theta_0+\theta) & 0 & \sin(\theta_0+\theta) \\ 0 & 1 & 0 \\ -\sin(\theta_0+\theta) & 0 & \cos(\theta_0+\theta) \end{bmatrix} \\ M_\phi &= \begin{bmatrix} \sin\phi & -\cos\phi & 0 \\ \cos\phi & \sin\phi & 0 \\ 0 & 0 & 1 \end{bmatrix} \\ M_t &= \begin{bmatrix} \cos(t_v+t_r) & 0 & \sin(t_v+t_r) \\ 0 & 1 & 0 \\ -\sin(t_v+t_r) & 0 & \cos(t_v+t_r) \end{bmatrix} \\ M_{\beta_p} &= \begin{bmatrix} -r\sin\beta_p\cos\phi \\ -r\sin\beta_p\sin\phi \\ r\cos\beta_p \end{bmatrix} \end{aligned} \tag{3}$$

This paper extends the rotor broadband noise prediction capability from a single rotor (Ref. 13) to multiple rotors on a vehicle. Equations (4) and (5) describe the coordinate transformations from the vehicle's global coordinate (X_2, Y_2, Z_2) with an origin at the vehicle hub to the rotor coordinate (X_1, Y_1, Z_1) with an origin at the rotor hub. Therefore, a user can conveniently input the global coordinate (X_2, Y_2, Z_2) relating a vehicle hub to an observer, and the program will perform the coordinate transformations internally to find the local coordinate (X, Y, Z) from Eqs. (2)–(5), which is necessary for the Amiet model (Ref. 7). The X_2Y_2 plane is parallel to the geographical ground shown in Fig. 6(a). Figure 6(b) shows the definitions of t_v and t_r, which were used in Eqs. (3) and (5). t_v is the vehicle tilt angle between the vehicle hub plane and the geographical ground, and t_r is the rotor tilt angle between the rotor hub plane and the vehicle hub plane.

$$\begin{bmatrix} X_1 \\ Y_1 \\ Z_1 \end{bmatrix} = M_{t_v} \left(\begin{bmatrix} X_2 \\ Y_2 \\ Z_2 \end{bmatrix} + M_{hub} \right) \tag{4}$$

$$M_{t_v} = \begin{bmatrix} \cos t_v & 0 & \sin t_v \\ 0 & 1 & 0 \\ -\sin t_v & 0 & \cos t_v \end{bmatrix} \quad \text{and} \quad M_{hub} = \begin{bmatrix} l_x \\ l_y \\ l_z \end{bmatrix} \tag{5}$$

The PSD of each section changes with the azimuth angle; hence, it is azimuthally averaged by Eq. (6). Note that the azimuthal averaging is not used for the calculations of amplitude modulation, which will be explained in the next section.

$$S_{pp} = \frac{N_B}{2\pi}\int_0^{2\pi}\left(\frac{\omega}{\omega_d}\right)^2 \overline{S}_{pp} d\phi, \tag{6}$$

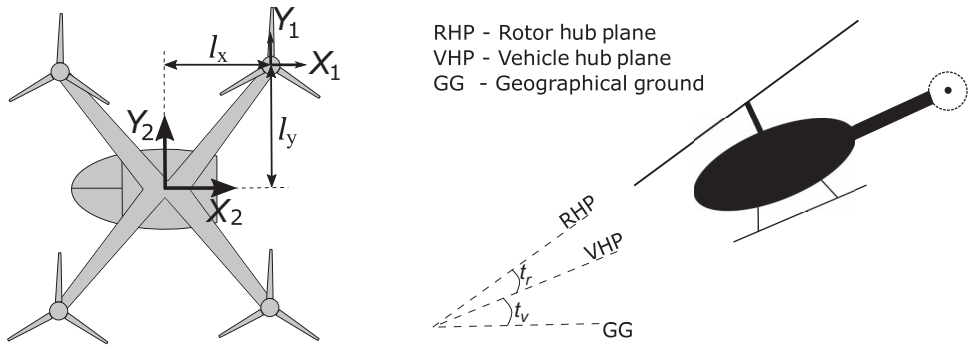

(a) (b)

Fig. 6. Multirotor vehicle coordinates: (a) rotor coordinate (X_1, Y_1, Z_1) and vehicle coordinate (X_2, Y_2, Z_2). The distance from rotor hub to vehicle hub is described by (l_x, l_y, l_z), and (b) rotor hub plane, vehicle hub plane, and geographical ground.

in which the Doppler-shifted frequency ω_d at the observer is related to the source frequency ω using

$$\frac{\omega_d}{\omega} = \frac{1}{1 + M_r\left(\frac{X}{R_s}\right)}. \tag{7}$$

Note that $M_r = \Omega r/c_o$ is the rotational Mach number of the blade section. X has the direction pointing from leading edge to trailing edge shown in Fig. 5 and computed by Eq. (2), and R_s is the distance between the blade section and an observer. Substituting Eqs. (1) and (7) into Eq. (6) and expanding the terms gives the acoustic PSD generated from a single side of each blade section as

$$S_{pp} = \left(\frac{\omega}{c_o}\right)^2 c^2 \triangle r \left(\frac{1}{32\pi^2}\right) \frac{N_B}{2\pi} \int_0^{2\pi} D_\phi |L|^2 l_r \Phi_{pp} d\phi \tag{8}$$

The directivity term is given as $D_\phi = (Z/\epsilon^2)^2$, where ϵ is defined in Eq. (1). The local coordinate of Z and ϵ must be found by taking the coordinate transformations in Eqs. (2) and (3) from the global coordinate. A detailed equation of the directivity term D_ϕ in terms of the global coordinate system (X_2, Y_2, Z_2) is provided in the Appendix.

The loading term L is given by Schlinker and Amiet (Ref. 8) as

$$|L| = \frac{1}{\Lambda}\left| e^{i2\Lambda}\left[1 - (1+i)\, E^*(2(\overline{K} + \overline{\mu}M + \overline{\gamma})) + e^{-i2\Lambda}\sqrt{\frac{K + \mu M + \gamma}{\mu x/\epsilon + \gamma}}\,(1+i)\, E^*\left(2\left(\overline{\mu}x/\epsilon + \overline{\gamma}\right)\right)\right]\right| \tag{9}$$

where $\Lambda = \overline{k}_x - \overline{\mu}x/\epsilon + \overline{\mu}M$, $K = \omega_d/U_c$, $\mu = \omega_d M/U\beta^2$, $\gamma^2 = (\mu/\epsilon)^2(x^2 + \beta^2 z^2)$, and E^* represents the complex conjugate of a Fresnel integral. In this study, the turbulence convective velocity and spanwise turbulence length scale are defined as $U_c = 0.8U_\infty$ and $l_r = 1.6U_c/\omega$, respectively.

The remaining wall pressure spectrum Φ_{pp} is obtained by a recently developed empirical wall pressure spectrum model for non-zero gradient flows, Lee's model (Ref. 15), as

$$\frac{\Phi_{pp}(\omega)U_e}{\tau_w^2 \delta^*} = \frac{\max(a, (0.25\beta_c - 0.52)a)\left(\frac{\omega\delta^*}{U_e}\right)^2}{\left[4.76\left(\frac{\omega\delta^*}{U_e}\right)^{0.75} + d^*\right]^e + \left[8.8R_T^{-0.57}\left(\frac{\omega\delta^*}{U_e}\right)\right]^{h^*}} \tag{10}$$

where $\beta_c = (\Theta/\tau_w)\,|dp/dx|$, $a = 2.28\Delta^2(6.13\Delta^{-0.75} + d)^e[4.2(\Pi/\Delta) + 1]$, $\Delta = \delta/\delta^*$, $\Pi = 0.8(\beta_c + 0.5)^{3/4}$, $e = 3.7 + 1.5\beta_c$, $d = 4.76(1.4/\Delta)^{0.75}[0.375e - 1]$, $R_T = (\delta/U_e)(\nu/u_\tau^2)$, $h^* = \min(3, (0.139 + 3.1043\beta_c)) + 7$, and if ($\beta_c < 0.5$), $d^* = \max(1.0, 1.5d)$, otherwise $d^* = d$.

Finally, the far-field SPL for one side of the ith section is calculated from the power spectral density S_{pp} as

$$\mathrm{SPL}_{i(U/L)} = 10\log_{10}\left(\frac{2\pi S_{pp}}{(2\times 10^{-5})^2}\right), \tag{11}$$

where U and L represent the upper and lower surfaces of an airfoil, respectively. The jth rotor's total SPL is logarithmically summed to be

$$\mathrm{SPL}_{\mathrm{rotor,j}} = 10\log_{10}\sum_{i=1}^{N_S}(10^{0.1\mathrm{SPL}_{iU}} + 10^{0.1\mathrm{SPL}_{iL}}), \tag{12}$$

where N_S is the total number of sections. Likewise, the total SPL of a vehicle with multiple rotors is given in Eq. (13), where N_R is the number of rotors.

$$\mathrm{SPL}_{\mathrm{vehicle}} = 10\log_{10}\sum_{j=1}^{N_R}(10^{0.1\mathrm{SPL}_{\mathrm{rotor,j}}}) \tag{13}$$

Amplitude modulation

Theoretically, the noise level is low when the blade is away from the observer and the level is high when the blade is close to the observer, so in the time duration, the noise level is fluctuating periodically, which is the logic of amplitude modulation. However, depending on its relative position to the observer, each section on a blade has a different corresponding observer time and noise level. Therefore, broadband noise from each blade section needs to be individually predicted before summing up to the total noise. Figure 7 shows the blade sections as the noise sources, where τ is the noise emission time and $\tau + R_s/c_0$ is the observer time. The emission time is associated with the angular velocity Ω and azimuthal angle ϕ by

$$\tau = \frac{\phi}{\Omega} \tag{14}$$

For the calculation of amplitude modulation, the azimuthal averaging is removed and the broadband noise of each blade section is recorded in time history, so Eq. (8) becomes Eq. (15), where $S_{pp,\phi}$ is the acoustic power spectrum density of one blade section at an azimuth angle.

$$S_{pp,\phi} = \left(\frac{\omega}{c_o}\right)^2 c^2 \triangle r \left(\frac{1}{32\pi^2}\right) D_\phi |L|^2 l_r \Phi_{pp} \tag{15}$$

In UCD-QuietFly, the observer time duration is a user's option, based on which the program determines the ending emission time while the starting emission time is kept at zero. At every emission time step, the

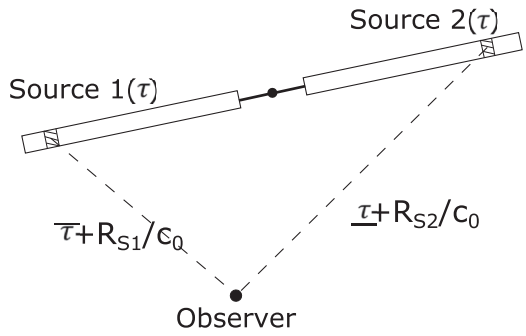

Fig. 7. Retarded time effect on amplitude modulation from each blade section as a noise source.

broadband noise from each blade section is calculated from Eq. (15), and based on the section's location its corresponding observer time is calculated. After the calculation of all sections and time steps, the total vehicle broadband noise as a function of observer time is interpolated and summed. As the output, the program generates the broadband noise SPL as a function of both frequency and observer time.

Results

This section presents the validation of UCD-QuietFly on broadband noise prediction on small-scale and VTOL-scale rotors. To investigate the importance of broadband noise for UAM VTOL aircraft, three six-passenger UAM VTOL vehicle designs (Ref. 21) are studied, and their broadband noise is compared to background noise measurements (Ref. 25). Regarding noise perception, the amplitude modulation of broadband noise is studied for single-rotor and multirotor configurations. Finally, the broadband noise contours from an urban vertiport are predicted.

Validation

Due to the lack of noise measurements of actual VTOL vehicles with multiple rotors, the validation of UCD-QuietFly in this paper is performed on a small-scale two-bladed rotor and a midscale four-bladed rotor that are representations of VTOL rotors, while the validation of UCD-QuietFly on full-scale helicopters has been presented in Refs. 13 and 28. Table 2 shows the test conditions for the two rotors, the APC Slower Flyer 11×4.7 rotor and the 40% scale BO-105 rotor, and the predictions for the two rotors at various operating conditions are presented in Figs. 8. The APC rotor was tested in the NASA Langley's Structural Acoustic Loads and Transmission (SALT) anechoic chamber by Zawodny et al. (Ref. 17), who mounted the single rotor on a test stand and positioned the microphone in the acoustic far-field with an elevation angle of -45°. The acoustics measurements of the 40% scale BO-105 rotor was acquired by Brooks et al. (Ref. 24) in the Duits–Nederlandse Wind Tunnel, where the model was tested in the forward and hover flights. The narrow-band spectra of both measurements (Refs. 17, 24) were post-processed using the fast Fourier transformation. The good comparisons of UCD-QuietFly and the measurements at various speeds demonstrate the validity of UCD-QuietFly's prediction on different scaled rotors. The predictions catch the noise spectrum from the mid- to high-frequency range, where rotor broadband noise is dominant; in Figs. 8(b)–8(d), they also follow a trend of an increase in noise levels from low to high rotational speeds for the BO-105 rotor. In the APC rotor prediction in Fig. 8(a), a sharp peak in the predictions and measurements at high frequencies is attributed to the trailing-edge bluntness noise. It is expected that the predictions do not match the data at low frequencies at which other noise sources are important, including loading noise (Ref. 29) and turbulence ingestion noise (Refs. 24, 30). The computational time to obtain the noise level of one rotor for one observer is 65 s on a personal desktop computer with an Intel i7-9700 Processor, 8 cores and 16 GB RAM.

The frequency f (in Hz) of the energetic fluctuations in the boundary layer approaching the trailing-edge scales as $f\delta^*/U_\infty = 0.06$–$0.08$ (Ref. 31). For the APC rotor, this scaling law results in 16.9 kHz using the boundary layer thickness and flow velocity at the blade tip. On a 40% scale BO-105 rotor with the rotor radius of 2 m, this scaling law provides the peak frequency of trailing-edge noise of above 4.5 kHz based on the blade tip. This peak frequency is slightly higher than the peak frequency in Fig. 8(a). Although this scaling law cannot be directly used to estimate the peak frequency of rotor trailing-edge noise since rotor noise is contributed from multiple airfoil segments, it still provides a rough estimate of a frequency region of interest in terms of rotor trailing-edge noise. This frequency range is designated as mid- to high-frequency region in this paper since other broadband noise, such as turbulence ingestion noise or BWI noise, typically occurs at lower frequencies than trailing-edge noise. It is obvious this frequency region is case dependent since the peak frequency is different based on the velocity and boundary-layer displacement thickness. In addition, the peak frequency range can also be different depending on operating conditions. Although we do not argue that these noise sources are always the dominant sources at certain frequency ranges, their audible levels that exceed community background noise present a clear community disturbance.

It should be noted that the narrow-band measurement data (Refs. 24, 30) for the validation problems show that broadband noise is dominant at this frequency range with an absence of tonal noise so that the predicted results represent the measured airfoil self-noise very well.

Prediction of UAM VTOL aircraft

Figures 9–11 shows the one-third octave band broadband noise predictions from UCD-QuietFly for the three different six-passenger VTOL designs: quadcopter, side-by-side, and lift+cruise. The broadband noise from these three designs is compared to investigate the noise levels for the same mission specifications. Five different altitudes, from 50 to 1500 ft, are studied for the hover flight with the observer straightly underneath the rotor (elevation angle of -90°). Due to the dipole directivity shape

Table 2. Specifications of the rotors used for UCD-QuietFly validation

Rotor Name	APC Slow Flyer 11×4.7	BO-105 40% Scale
Rotor radius (m)	0.14	2.0
Number of blades	2	4
Observer distance to hub (m)	1.095	7.14
Observer elevation angle (deg)	− 45	90
Airfoil	E63(root)/ClarkY(tip)	NACA 23012

The sign convention of the elevation angle is defined in Fig. 5

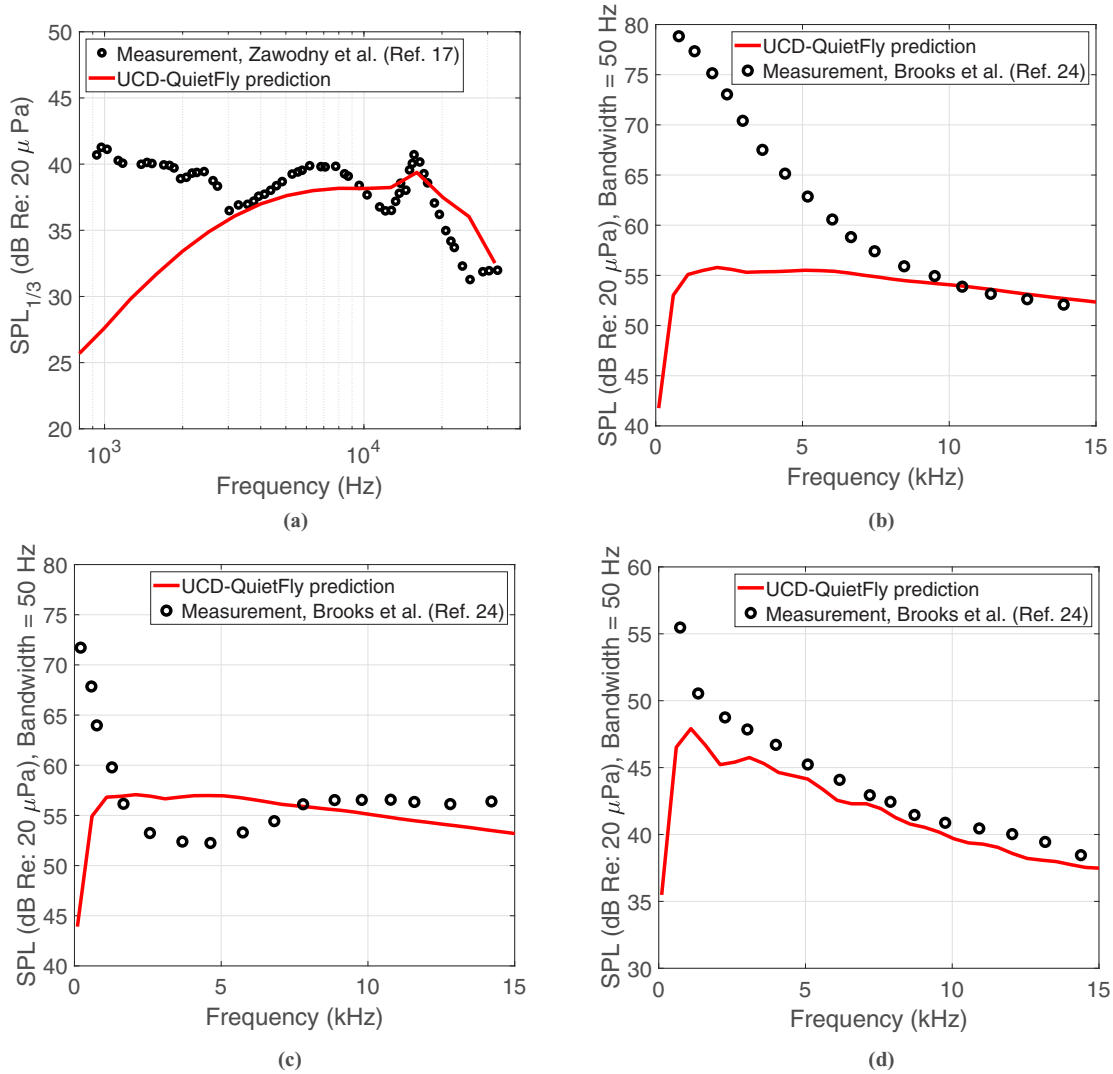

Fig. 8. Validations of UCD-QuietFly on rotors. (a) APC Slow Flyer 11×4.7, RPM = 3600, $\mu = 0.0$, (b) BO-105 40% scale, RPM = 1050, $\mu = 0.0$, $\alpha_{tpp} = -20°$, $C_T = 0.0$, (c) BO-105 40% scale, RPM=1050, $\mu = 0.086$, $\alpha_{tpp} = -20°$, $C_T = 0.0044$, and (d) BO-105 40% scale, RPM = 525, $\mu = 0.173$, $\alpha_{tpp} = -10°$, $C_T = 0.044$.

of rotor broadband noise (Ref. 13), this overhead position has the maximum broadband noise level. Although the ground noise reflection effect is not included in this paper, this may increase the noise levels further. In each figure, the community background noise measurements (Ref. 25) are included for reference. For the quadrotor at the highest studied altitude of 1500 ft, the broadband noise is audible above 0.7 kHz in a rural area, above 2 kHz in a community park, above 3.5 kHz in a residential community, and above 6 kHz in a highway area. Compared to that at 1500 ft, as the quadrotor altitude is decreased, the noise level is increased by about 4 dB at 1000 ft, 10 dB at 500 ft, 15 dB at 250 ft, and 30 dB at 50 ft. At the typical altitude of a vertiport of 50 ft, quadcopter noise is not masked for a large frequency range (>0.4 kHz) even in the freeway environment. Note that broadband noise is predicted from one quadrotor, and a higher noise level is observed with multiple vehicles, which is presented in the next section. In sum, broadband noise of multirotor VTOL vehicles stands out in the mid- to high-frequency range, where VTOL broadband noise is not masked by the community background noise.

Compared to the quadrotor design, the side-by-side VTOL generates slightly less broadband noise (2 dB) in the entire frequency range, but the high-frequency noise is important to human perception for its audibility in urban areas. Regarding the lift+cruise design, its high-frequency broadband noise remains the same importance as the quadrotor design while low- to mid-frequency broadband noise is increased.

To make more direct comparisons, Figure 12 shows the community equivalent sound exposure level (L_{eq}) measured by Begault (Ref. 25) and the overall sound pressure level (OASPL) predicted from UCD-QuietFly for the three UAM VTOL designs, where L_{eq} and OASPL are mathematically the same since the broadband is statistically stationary or not time varying. In this paper, the OASPL is calculated in the frequency range from 0.1 to 10 kHz. Comparing the overall SPL, in the freeway environment, broadband noise from the UAM VTOL vehicles are important at 50 ft altitude, or a vertiport's height. In the residential community, broadband noise is important at an altitude of 250 ft. In the community park, broadband noise is important for the quadcopter vehicle at 1000 ft, the side-by-side vehicle at 500 ft, and the lift+cruise vehicle at 1000 ft. Finally, in the rural area, broadband noise is important for all vehicles at 1500 ft. However, OASPL represents the general importance, while the importance of high-frequency noise compared to all measured environments cannot be neglected as shown in Figs. 9–11. Although our

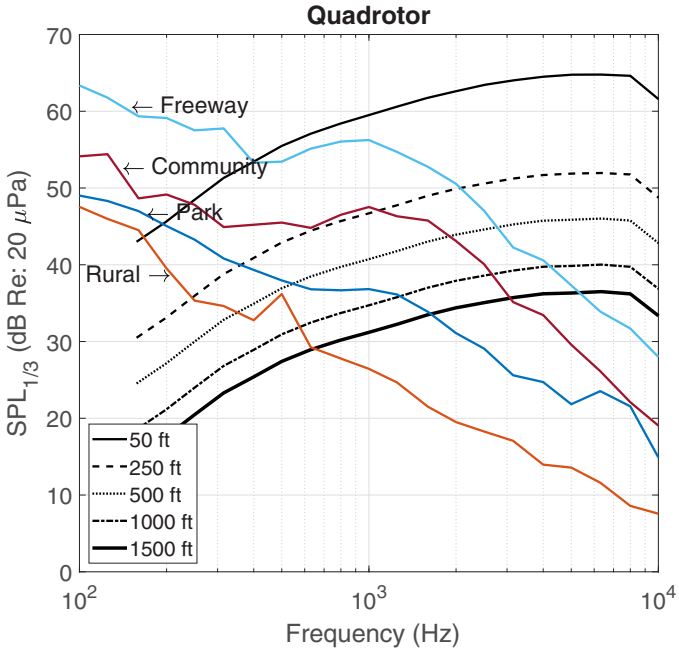

Fig. 9. Quadrotor VTOL broadband noise prediction from UCD-QuietFly compared to community background noise (Ref. 25). Peak-level frequency = 6 kHz.

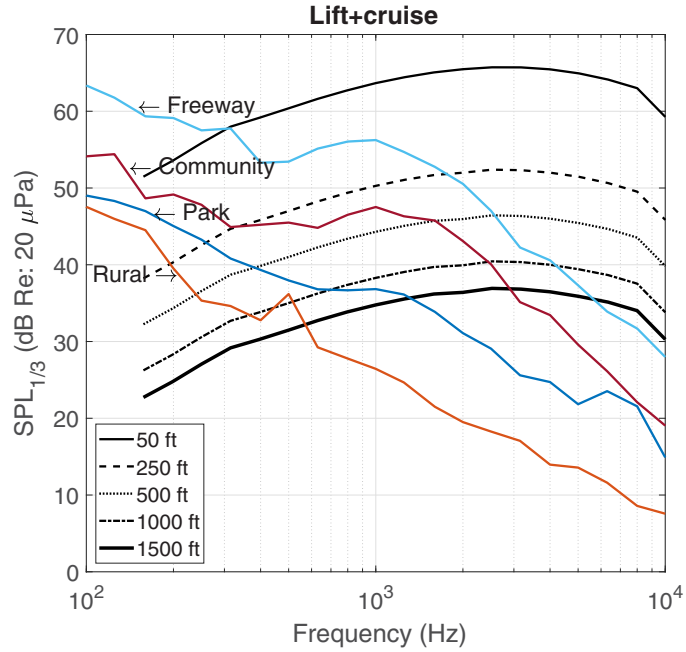

Fig. 11. Lift+cruise VTOL broadband noise prediction from UCD-QuietFly compared to community background noise (Ref. 25). Peak-level frequency = 3 kHz.

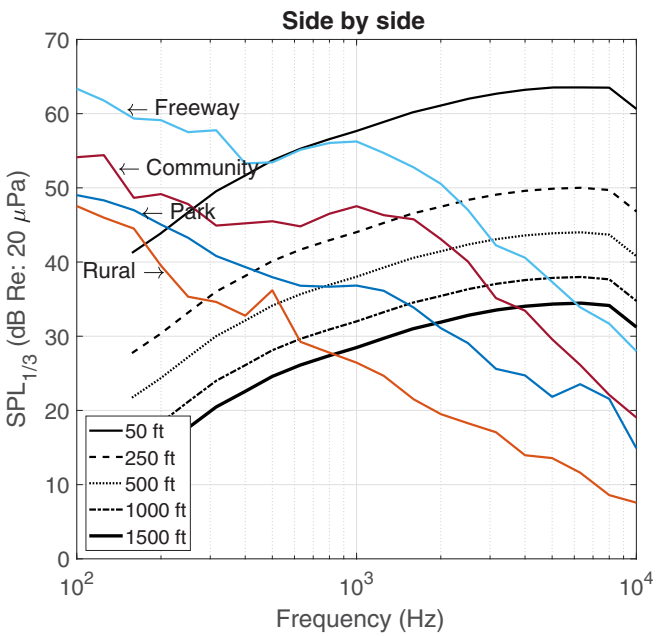

Fig. 10. Side-by-side VTOL broadband noise prediction from UCD-QuietFly compared to community background noise (Ref. 25). Peak-level frequency = 7 kHz.

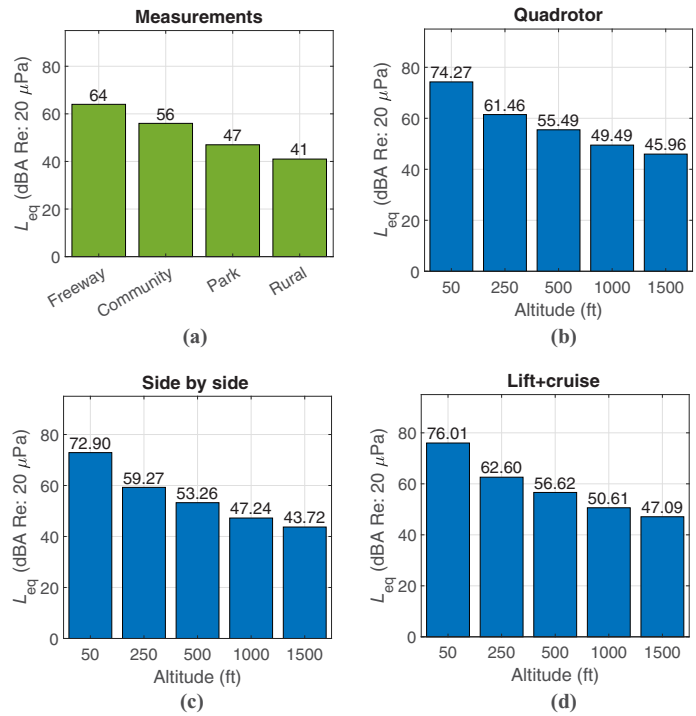

Fig. 12. Equivalent sound exposure level measurement and overall SPL prediction for: (a) community background noise (Ref. 25), (b) quadrotor, (c) side-by-side, and (d) lift+cruise.

research demonstrates the importance of high-frequency UAM VTOL broadband noise, low-frequency UAM VTOL noise can also be audible from other noise sources, such as BVI noise (Refs. 23, 22).

Comparing the broadband noise levels from the three UAM VTOL designs, it is shown that the design with more rotors generates higher broadband noise in the same mission specifications. To further investigate the effect of the number of rotors on broadband noise, the number of rotors is varied with the lift+cruise VTOL being a base design, where the rotor tip speed and total swept area from multiple rotorsare kept the

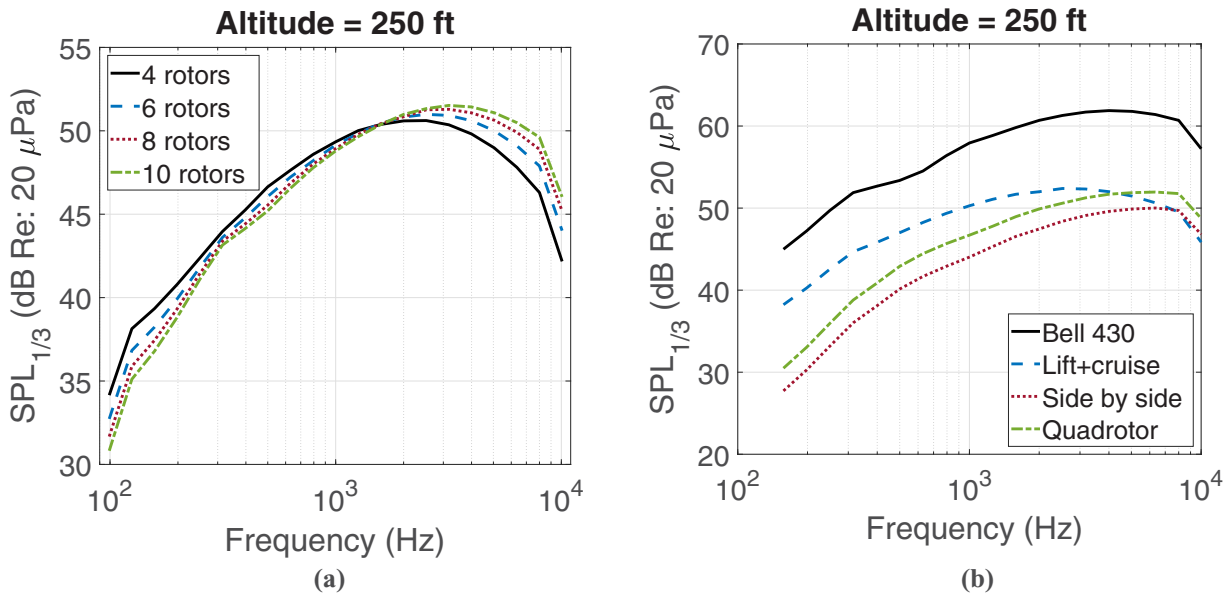

Fig. 13. Comparisons of UAM VTOL designs: (a) effect of changing the number of rotors by keeping the same tip Mach number and the same total swept area from multiple rotors and (b) broadband noise of conventional helicopter Bell 430 compared to multirotor UAM VTOLs.

same. As the number of rotors increases, the blade radius of each rotor is reduced and rotational speed is increased. The one-third octave band SPLs from a various number of rotors are shown in Fig. 13(a). While the increasing number of rotors increases high-frequency broadband noise, low-frequency noise is decreased. This trend can be explained by the fact that reducing the blade radius with multirotors results in decreasing low-frequency noise while maintaining the same high-frequency noise on a single rotor (Ref. 13). However, high-frequency noise increases as added rotors generate more trailing-edge noise. As noise from multiple rotors with reduced blade radius is combined, the overall effect gives an increase in high-frequency noise and a decrease in low-frequency noise. In Fig. 13(b), the three UAM VTOL conceptual designs are seen to have lower broadband noise than the conventional helicopter Bell 430 that has a similar payload as the conceptual designs. Hovering at the altitude of 250 ft, the broadband noise of a Bell 430 helicopter is about 10 dB higher than that of the UAM VTOL conceptual designs, which indicates the noise benefit of operating multirotor VTOL at low tip speeds. Uber recommended a UAM noise requirement of 15 dB lower than helicopter noise (Ref. 32). This 15 dB noise reduction requirement might be challenging in terms of trailing-edge noise.

Amplitude modulation

The amplitude modulation of UAM VTOL aircraft broadband noise is investigated to find its importance for various observer distances and vehicle designs. In the current study, the rotors on a vehicle are assumed to be in phase. It would be interesting to study the amplitude modulations with varying rotor phases. On a two-bladed UH-1B single rotor, the broadband noise spectrum in time history is presented for various observer distances in Fig. 14, where the elevation angle is fixed at -45°. The ending time is 1 s for the four cases, and the starting time is 0.4 s. Figure 14 shows that the broadband noise level periodically varies with time for the entire frequency range. As the observer distance is increased, the overall noise level is decreased while the amplitude modulation remains the same patterns. In addition, within the same time duration, the number of peaks present remains unchanged for different observer radial distances. Such periodic variations are caused by the variation of source-to-observer distance as well as the Doppler effect; the blade moves away from the observer with decreasing noise and towards the observer with increasing noise. Therefore, the period of amplitude modulation is associated with the number of blades and the number of rotors, as well as the rotational speed.

To further investigate the effects of the number of blades and the number of rotors on the broadband noise amplitude modulation at the same rotational speed, broadband noise in the time history is predicted for the three VTOL designs in Fig. 15. The side-by-side, quadrotor, and lift+cruise VTOLs have 2, 4, and 8 rotors, and 8, 12, and 16 blades in total. The observer is located at 44 ft (R_0) and -45° elevation angle from the vehicle hub.

Figure 16 shows the OASPL peak-to-peak amplitudes and time history of OASPL of the UH-1B single rotor at various observer distance. It is found that increasing an observer distance reduces the amplitude while the period remains the same. To explain this observation, as the observer–hub distance is increased, the relative difference between the observer–source 1 distance and the observer–source 2 distance in Fig. 7 becomes smaller. For a fixed observer–hub distance (R_0), Fig. 17 shows the OASPL peak-to-peak amplitudes and time history of OASPL for different vehicle configurations, which include the UH-1B helicopter and the three UAM VTOL designs. It is demonstrated that the multirotor designs have much smaller OASPL peak-to-peak amplitudes than the single rotor. Figure 17(b) shows that as the number of blades increases, the modulation period and the peak-to-peak amplitude are both reduced. Within a time duration of 0.2 s, the single rotor has two periods, the side-by-side VTOL has six periods, the quadrotor VTOL has seven periods, and the lift+cruise VTOL has nine periods, although they are not clearly shown in Fig. 17(b). Therefore, increasing the number of blades increases the number of amplitude modulations, which is similar to the blade passing frequency of tonal noise being increased with the number of blades. Since the observer location is kept at 44 ft, however, a rotor blade with a smaller radius with multiple rotors has a smaller difference between the largest and smallest source-to-observer distances as the blade rotates away and towards the observer, so the peak-to-peak amplitude is smaller. Therefore, more blades result

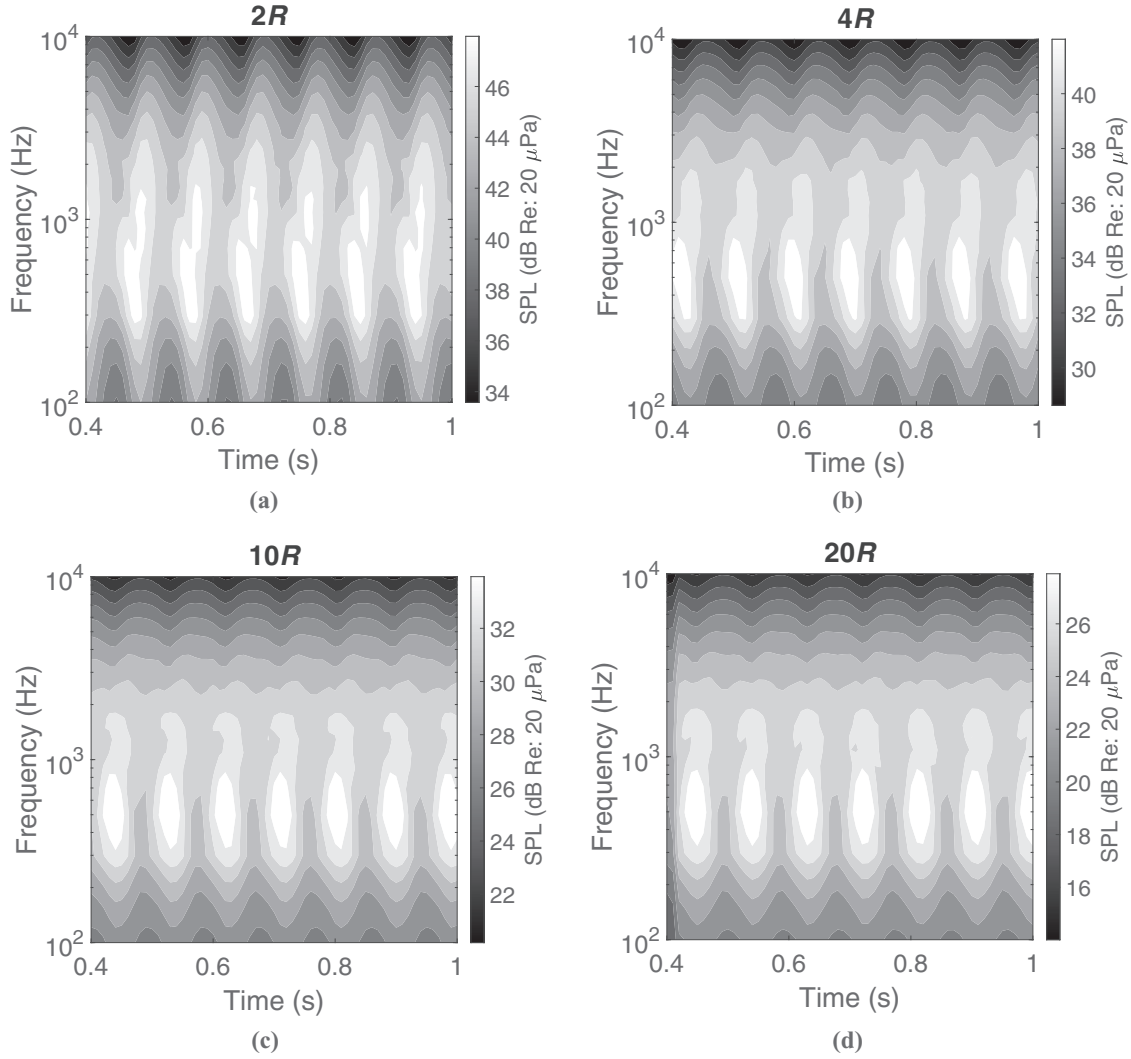

Fig. 14. Broadband noise spectrum of a UH-1B helicopter in time history for observer distances at an elevation angle of −45 deg: (a) 2*R*, (b) 4*R*, (c) 10*R*, and (d) 20*R*.

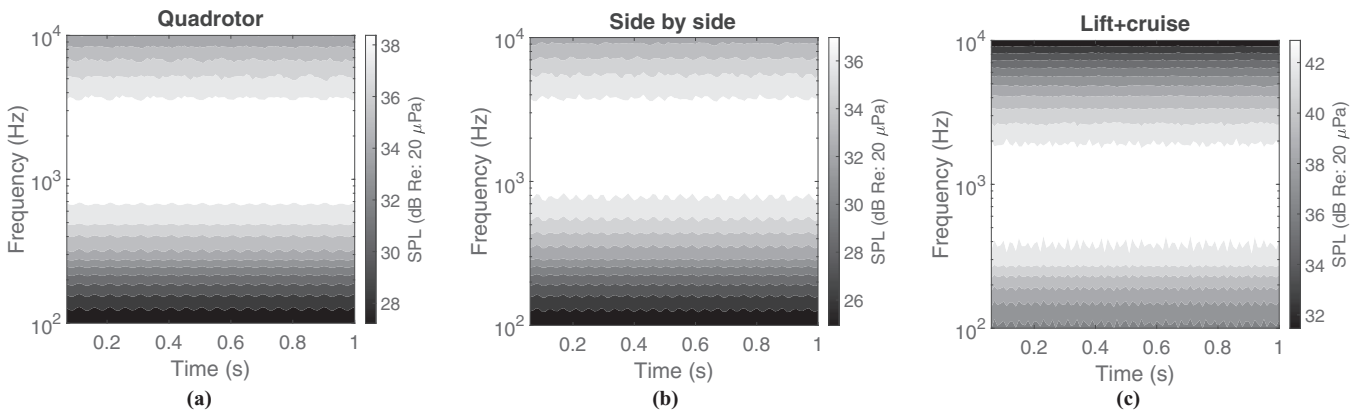

Fig. 15. Broadband noise spectrum of multirotor vehicles in time history: (a) quadcopter, (b) side-by-side, and (c) lift+cruise.

in more noise peaks but smaller amplitudes of the modulation. Different from the simple periodic amplitude modulations for the single rotor, the multirotors have the irregular peaks, since their amplitude modulations are combined from multiple periodic modulations of each rotor with phase differences. In conclusion, the amplitude modulation of rotorcraft broadband noise becomes weak when the source-to-observer distance is large; in our case, the peak-to-peak amplitude of OASPL is less than 1 dB when an observer is four rotor radii from the rotor hub. For a fixed observer location, the amplitude modulation is less important for a larger number of blades. Thus, one acoustic advantage

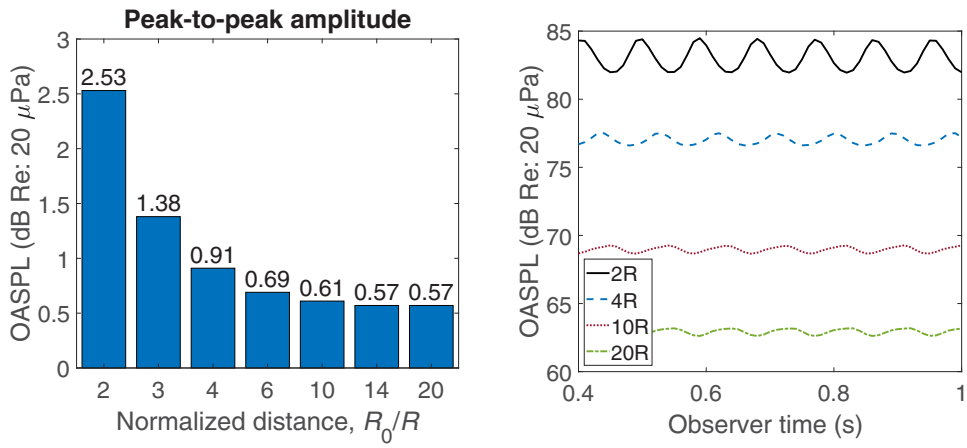

(a) (b)

Fig. 16. Predicted UH-1B helicopter amplitude modulation: (a) peak-to-peak amplitude vs. observer distance and (b) OASPL in time history for different observer distances.

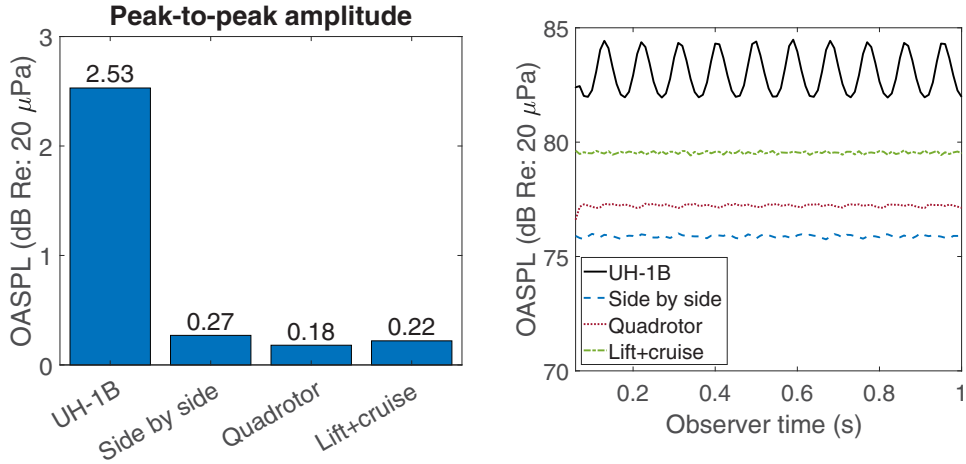

(a) (b)

Fig. 17. Predicted amplitude modulations of different vehicle designs: (a) peak-to-peak amplitudes for four designs and (b) OASPL in time history for four designs.

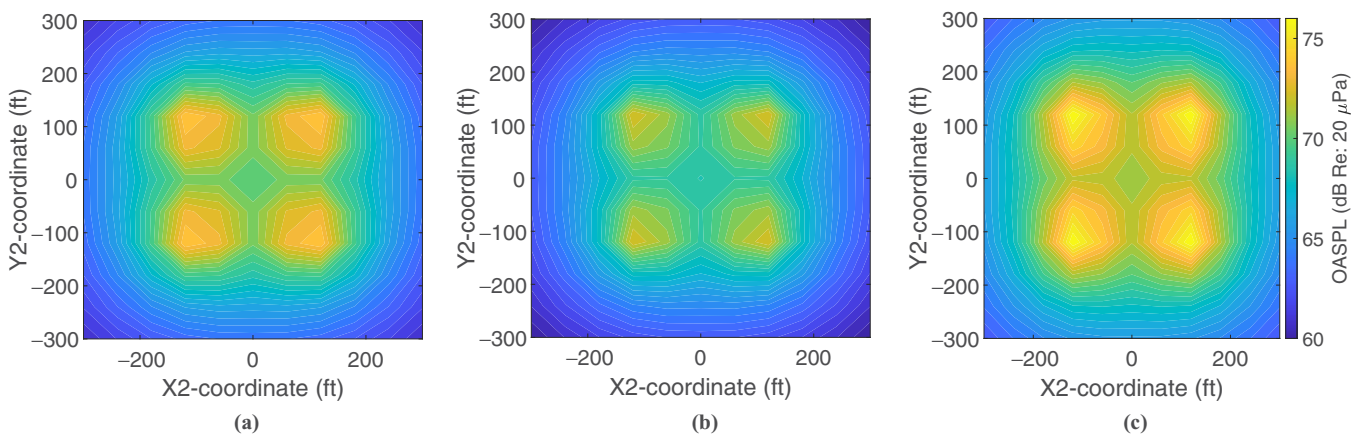

(a) (b) (c)

Fig. 18. Predicted broadband noise OASPL from the 4-FATO Gannett Fleming (Ref. 26) vertiport: (a) quadcopter, (b) side-by-side, and (c) lift+cruise.

of VTOL designs with more rotors and more blades is that they have less annoying broadband noise characteristics associated with amplitude modulation.

Vertiport

Built in urban areas for vehicles to vertically take-off and land, vertiports are relevant to the communities' noise perception for their vicinities of residential areas. The Gannett Fleming vertiport (Ref. 26) is considered for the evaluation of broadband noise from multiple UAM VTOL designs. Four UAM VTOL vehicles are operated simultaneously at the four final approach and take-off areas (FATO) (Ref. 33) at the altitude of 40 ft, and the overall SPLs are predicted for a map of observer locations on the ground, where the noise scattering effects from the vertiport building are neglected. The noise predictions for quadcopter, side-by-side, and lift+cruise VTOLs are shown in Fig. 18, respectively. The lift-cruise design has higher broadband noise than the quadrotor design, and the side-by-side design has the lowest broadband noise. This result is consistent with an earlier finding that more blades generate a higher amplitude of broadband noise. Directly below the FATOs are the four local noise maxima, with each vehicle accounting for each noise maximum.

Conclusions

Urban air mobility VTOL broadband noise has been studied using an updated UCD-QuietyFly program, which includes the coordinate transformations from single to multiple rotors. The broadband noise amplitude modulation is analyzed to study the noise characteristics. UCD-QuietFly is validated against measured noise levels for two scaled rotors. Key findings are concluded as follows:

1) Broadband noise of UAM VTOL vehicles is important in the mid- to the high-frequency range (frequency > 1 kHz). Comparing to the noise measurements shows that mid- to high-frequency broadband noise of UAM VTOL aircraft is not masked in urban community environments, and future investigation on broadband noise reduction is recommended for UAM VTOLs.

2) With the same payload operating at the altitude of 250 ft, multirotor UAM vehicle broadband noise is about 10 dB lower than conventional single rotor helicopter noise. However, 10 dB noise reduction may not be sufficient to meet public acceptance of UAM vehicles. For the same mission specifications, broadband noise of the quadrotor design is slightly higher than that of the side-by-side design, and the lift-cruise design has a considerable broadband noise increase compared to the other two designs.

3) Amplitude modulation of broadband noise on a single rotor is weak when the observer distance is larger than four rotor radii at an elevation angle of -45°. Increasing the number of blades increases the number of amplitude modulations, but with reduced amplitudes. Multirotor vehicles have weaker amplitude modulations, since the blade radius is decreased compared to the single rotors with the same swept area, which is a benefit of choosing multirotor designs.

4) Noise contours from a vertiport design demonstrate the increase in broadband noise level when multiple UAM VTOL vehicles are operated simultaneously.

Acknowledgements

This research was funded by Hyundai Motor Company for a project of UAM aircraft broadband noise prediction.

Appendix

The expanded form of the directivity term D_ϕ is shown in Eq. (2), which is obtained by performing the coordinate transformations in Eqs. (2)–(5).

$$\begin{aligned} D_\phi = A_1/\{&[\sin(\theta_0+\theta)\cdot A_3 - \cos(\theta_0+\theta)\cdot\cos\beta_p\cdot A_4 \\ &+ \cos(\theta_0+\theta)\sin\beta_p\cdot A_2]^2 + A_1 \\ &+ [\sin\beta_p\cdot A_4 + \cos\beta_p\cdot A_2]^2\}^2 \end{aligned} \tag{A1}$$

A_1, A_2, A_3, and A_4 in Eq. (A1) are shown as follows for clarity:

$$\begin{aligned} A_1 = &[\cos(\theta_0+\theta)\cdot A_3 + \sin(\theta_0+\theta)\cos\beta_p\cdot A_4 \\ &- \sin(\theta_0+\theta)\sin\beta_p\cdot A_2]^2 \end{aligned} \tag{A2}$$

$$\begin{aligned} A_2 = &\cos(t_r+t_v)[\cos t_v(l_x+X_2) + \sin t_v(l_z+Z_2)] + \sin(t_r+t_v) \\ &\times [\cos t_v(l_z+Z_2) - \sin t_v(l_x+X_2)] - r\cos\phi\sin\beta_p \end{aligned} \tag{A3}$$

$$\begin{aligned} A_3 = &\cos(t_r+t_v)[\cos t_v(l_z+Z_2) - \sin t_v(l_x+X_2)] \\ &- \sin(t_r+t_v)(\cos t_v(l_x+X_2) + \sin t_v(l_z+Z_2)) + r\cos\beta_p \end{aligned} \tag{A4}$$

$$A_4 = l_y + Y_2 - r\sin\beta_p\sin\phi \tag{A5}$$

References

[1]Intaratep, N., Alexander, W., Devenport, W., Grace, S. M., and Dropkin, A., "Experimental Study of Quadcopter Acoustics and Performance at Static Thrust Conditions," AIAA 2016-2873, Proceedings of 22nd AIAA/CEAS Aeroacoustics Conference, Lyon, France, May 30–June 1, 2016.

[2]Zawodny, N., and Boyd, D., "Investigation of Rotor-Airframe Interaction Noise Associated with Small-Scale Rotary-Wing Unmanned Aircraft Systems," *Journal of the American Helicopter Society*, Vol. 65, (1), 2020, pp. 1–17.

[3]Brooks, T., Pope, D., and Marcolini, M., "Airfoil Self-noise and Prediction," NASA RP 1218, 1989.

[4]Ffowcs Williams, J., and Hall, L., "Aerodynamic Sound Generation by Turbulent Flow in the Vicinity of a Scattering Half Plane," *Journal of Fluid Mechanics*, Vol. 40, (4), 1970, pp. 657–670.

[5]Lighthill, M., "On Sound Generated Aerodynamically, I. General Theory," *Proceedings of the Royal Society*, Vol. A211, 1952, pp. 564–587.

[6]Curle, N., "The Influence of Solid Boundaries upon Aero-Dynamic Sound," *Proceedings of the Royal Society*, Vol. A231, 1955, pp. 505–514.

[7]Amiet, R., "Noise Due to Turbulent 5 Flow Past a Trailing Edge," *Journal of Sound and Vibration*, Vol. 47, (3), 1976, pp. 387–393.

[8]Schlinker, R., and Amiet, R., "Helicopter Rotor Trailing Edge Noise," NASA RP 3470, 1981.

[9]Ffowcs Williams, J., and Hawkings, D., "Theory Relating to the Noise of Rotating Machinery," *Journal of Fluid Mechanics*, Vol. 10, (1), 1969, pp. 10–21.

[10]Kim, Y., and George, A., "Trailing-Edge Noise from Hovering Rotors," *AIAA Journal*, Vol. 20, (9), 1982, pp. 1167–1174.

[11]Blandeau, V., and Joseph, P., "Validity of Amiet·s Model for Propeller Trailing-Edge Noise" *AIAA Journal*, Vol. 49, (5), 2011, pp. 1057–1066.

[12]Goody, M., "Empirical Spectral Model of Surface Pressure Fluctuations," *AIAA Journal*, Vol. 42 (9), 2004, pp. 1788–1794.

[13]Li, S., and Lee, S., "Prediction of Rotorcraft Broadband Trailing-Edge Noise and Parameter Sensitivity Study," *Journal of the American Helicopter Society*, Vol. 65, (4), 2020, pp. 1–14.

[14]Drela, M., "XFOIL: An Analysis and Design System for Low Reynolds Number Airfoils," in *Low Reynolds Number Aerodynamics*, edited by T. J. Mueller, Lecture Notes in Engineering, Vol. 54, Springer, Berlin, 1989, pp. 1–12.

[15]Lee, S., "Empirical Wall-Pressure Spectral Modeling for Zero and Adverse Pressure Gradient Flows," *AIAA Journal*, Vol. 56, (5), 2018, pp. 1818–1829.

[16]Lee, S., and Shum, J., "Prediction of Airfoil Trailing-Edge Noise Using Empirical Wall-Pressure Spectrum Models," *AIAA Journal*, Vol. 57, (3), 2019, pp. 888–897.

[17]Zawodny, N., Boyd, D., and Burley, C., "Acoustic Characterization and Prediction of Representative, Small-Scale Rotary-Wing Unmanned Aircraft System Components," Proceedings of the 72nd Annual Forum of the American Helicopter Society, West Palm Beach, FL, May 17–19, 2016.

[18]Pettingill, N., and Zawodny, N., "Acoustic Characterization and Prediction of Representative, Small Scale Rotary-Wing Unmanned Aircraft System Components," Proceedings of the Vertical Flight Society 75th Annual Forum & Technology Display, Philadelphia, PA, May 13–16, 2019.

[19]Christian, A., Caston, J., and Greenwood, E., "Regarding the Perceptual Significance and Characterization of Broadband Components of Helicopter Source Noise," Proceedings of the Vertical Flight Society 75th Annual Forum & Technology Display, Philadelphia, PA, May 13–16, 2019.

[20]Johnson, W., Silva, C., and Solis, E., "Concept Vehicles for VTOL Air Taxi Operations," Proceedings of the American Helicopter Society Technical Conference on Aeromechanics Design for Transformative Vertical Flight, San Francisco, CA, January 16–19, 2018.

[21]Silva, C., Johnson, W., Solis, E., Patterson, M., and Antcliff, K., "VTOL Urban Air Mobility Concept Vehicles for Technology Development," AIAA 2018-3847, Proceedings of the 2018 AIAA Aviation Forum, Atlanta, GA, June 25–29, 2018.

[22]Jia, Z., and Lee, S., "Computational Study of Aerodynamics and Acoustics for Quadrotor eVTOL Aircraft," Proceedings of the 2020 VFS Aeromechanics for Advanced Vertical Flight Technical Meeting, San Jose, CA, January 21–23, 2020.

[23]Jia, Z., and Lee, S., "Acoustic Analysis of a Quadrotor eVTOL Design via High-Fidelity Simula- tions," AIAA 2019-2631, Proceedings of the 25th AIAA/CEAS Aeroacoustics Conference, Delft, The Netherlands, May 20–23, 2019.

[24]Brooks, T., Marcolini, M., and Pope, D"Main Rotor Broadband Noise Study in the DNW," *Journal of the American Helicopter Society*, Vol. 34, (2), 1989, pp. 3–12.

[25]Begault, D., "Ambient Noise Measurement for UAM Metric Analysis and Research," Proceedings of the Acoustics and Urban Air Mobility Technical Working Group Meeting, Hampton, VA, April 9–11, 2019.

[26]Gary, A., and Goyal, R., "Ambient Noise Measurement for UAM Metric Analysis and Research," Proceedings of the Acoustics and Urban Air Mobility Technical Working Group Meeting, Cleveland, OH, October 22–24, 2019.

[27]Landahl, M., *Unsteady Transonic Flows*, Pergamon Press, London, 1961.

[28]Li, S., and Lee, S., "A Machine Learning-Based Fast Prediction of Rotorcraft Broadband Noise," AIAA 2020-2588, Proceedings of the 2020 AIAA Aviation Forum, Virtual Event, June 15–19, 2020.

[29]Jia, Z., Lee, S., Sharma, K., and Brentner, K., "Aeroacoustic Analysis of a Lift-Offset Coaxial Rotor Using High-Fidelity CFD/CSD Loose Coupling Simulation," *Journal of the American Helicopter Society*, **65**, 012011 (2020).

[30]Brooks, T., and Burley, C., "Blade Wake Interaction Noise for a Main Rotor," *Journal of the American Helicopter Society*, Vol. 49, (1), 2004, pp. 11–27.

[31]Colonius, T., and Lele, S. K., "Computational Aeroacoustics: Progress on Nonlinear Problems of Sound Generation," *Progress in Aerospace Sciences*, Vol. 40, (6), 2004, pp. 345–416.

[32]Holden, J., and Goel, N., "Fast-Forwarding to a Future of On-Demand Urban Air Transportation," White Paper, Uber, 2016.

[33]Vasick, P., and Hansman, J., "Development of Vertiport Capacity Envelopes and Analysis of Their Sensitivity to Topological and Operational Factors," AIAA 2019-0526, Proceedings of the 2019 AIAA SciTech Forum, San Diego, CA, January 7–11, 2019.